Supplementary Information: Light focusing and additive manufacturing through highly scattering media using upconversion nanoparticles

Qianyi Zhang[1], Antoine Boniface[1], Virendra K. Parashar[2], Viola Sgarminato[1], Jorge Madrid-Wolff[1], Martin A. M. Gijs[2], and Christophe Moser[1,*]

[1] Laboratory of Applied Photonics Devices, School of Engineering, Institute of Electrical and Micro Engineering, Ecole Polytechnique Fédérale de Lausanne, Lausanne, Switzerland

[2] Laboratory of Microsystems LMIS2, School of Engineering, Institute of Electrical and Micro Engineering, Ecole Polytechnique Fédérale de Lausanne, Lausanne, Switzerland

[*]To whom correspondence should be addressed. e-mail: christophe.moser@epfl.ch

S1: TEM images of UCNPs

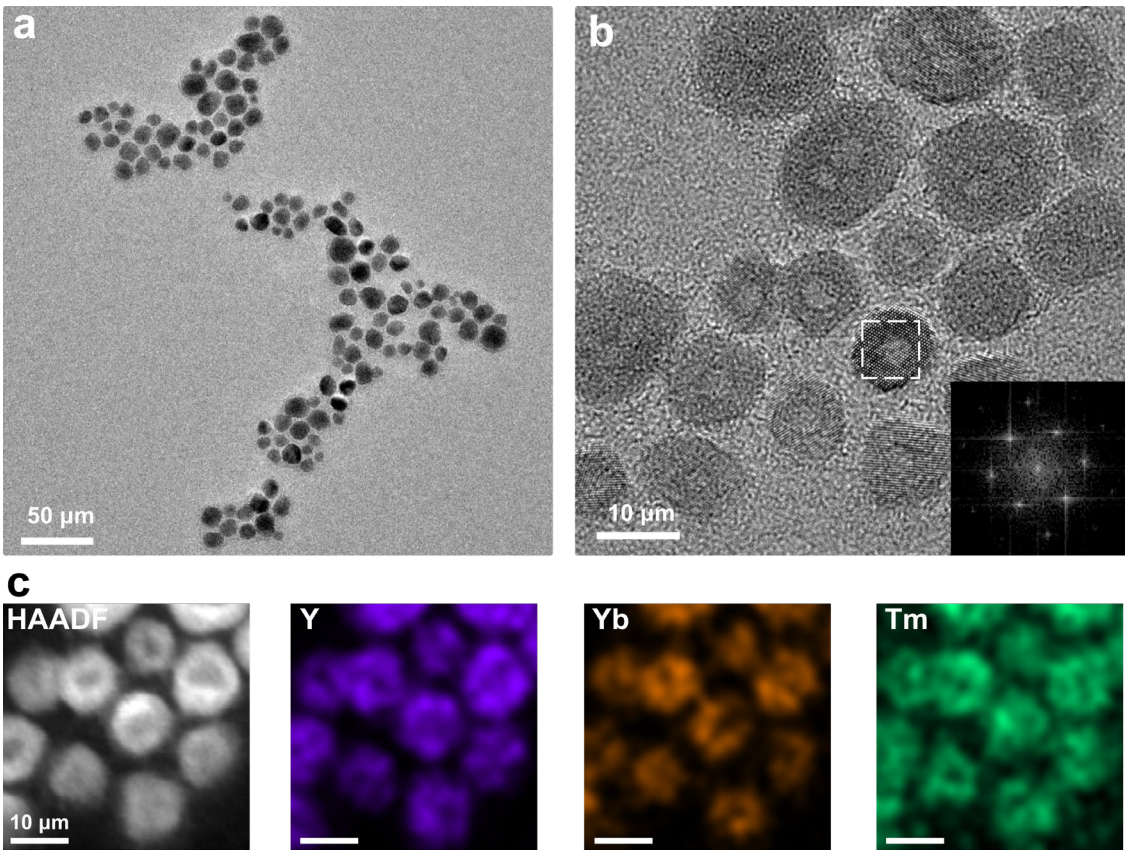

Fig. S1. Microstructural characterization of synthesized UCNPs. **a** TEM images of $NaYF_4$:Yb^{3+},Tm^{3+}@$NaYF_4$. **b** High-resolution TEM image of core-shell nanoparticles, with the Fourier-transform diffraction pattern of the highlighted region shown in the inset. **c** HAADF-STEM image and corresponding EDX elemental mapping images of core-shell nanoparticles.

Transmission Electron Micrograph, Fig. S1a, revealed uniform size ~10 nm of studied core-shell $NaYF_4$: Yb^{3+},Tm^{3+}@$NaYF_4$ upconversion nanoparticles. A magnified view and electron diffraction, Fig. S1b, indicate high crystallinity of these UCNPs along with uniform size: core ($NaYF_4$: Yb^{3+},Tm^{3+}) diameter of 3-4 nm and shell ($NaYF_4$) thickness of 3 nm. We have purposely taken a TEM sample area to understand if there is any agglomeration of core particles during shell deposition process. Fig. S2b shows distinguished, uniform two core particles in a shell, confirming core particles without any agglomeration inside the shell. UCNPs have uniform Ln element distribution (Fig. S2c). Precise control over the core size, as well of shelling thickness is essential for an efficient lanthanide energy transfer and upconversion quantum yield[1,2]. TEM analysis verified the precise size and uniform distributed Ln elements in our core-shell particles, making them suitable for the current study.

S2: Verification of LAP coating

FTIR spectrum of UCNP shows two absorption peaks at ~3500 and ~ 1600 cm^{-1}, which come from water residues in the sample. In contrast, FTIR spectrum of UCNP@LAP shows multiple absorption peaks at ~3000 and 500-1700 cm^{-1}, indicating the presence of LAP in the sample. LAP coating is verified in Zeta potential analysis. After coating with LAP, Zeta potential of nanoparticles decreases from +41.8±6.02 mV to +35.3±5.32 mV. This slight decrease is because of the weak electrostatic interactions between UCNP and LAP and thin-layer coating.

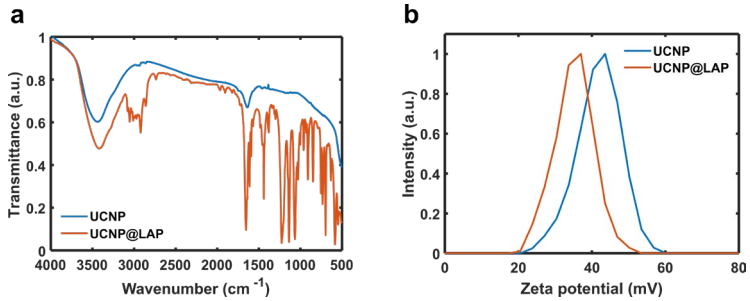

Fig. S2. **a** FTIR spectra of UCNPs and coated UCNPs (UCNP@LAP). **b** Zeta potentials of UCNPs and coated UCNPs.

S3: NIR light distribution on DMD

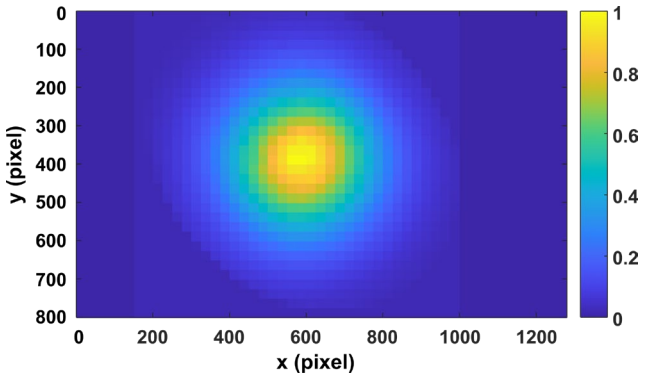

Fig. S3. Normalized NIR light distribution on DMD. It is calibrated by flipping each segment (25 × 25 pixels) of DMD and measuring the output power change.

S4: DMD encoding strategy

In the iterative algorithm, the search patterns are grayscale patterns (between 0 and 1) with a matrix size of 32 × 17. Then each element of the pattern is encoded in a rectangular segment (25 × 50 pixels) on DMD. The encoding strategy is shown in Fig. S4. First, this element is encoded with 5 binary pixels using a lookup table illustrated in Fig. S4a. Then these 5 pixels are expanded to a segment by repeating each pixel for 10 times in *y*-axis and 25 times in the *x*-axis. For example, an element 0.25 will be encoded by a segment pattern shown in Fig. S4b. Fig. S4c shows a DMD binary pattern encoding a grayscale search pattern with this strategy.

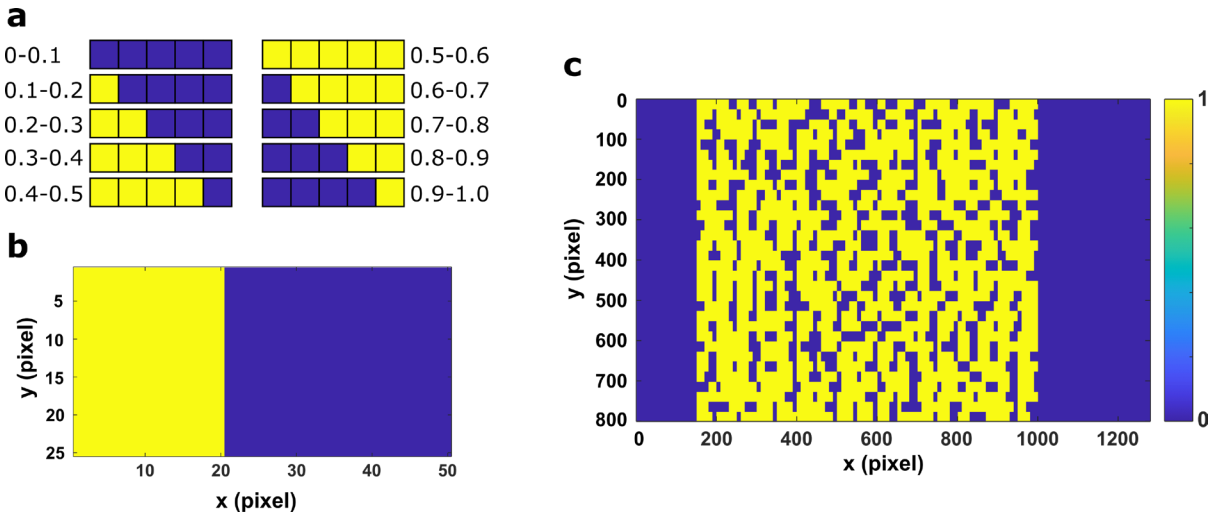

Fig. S4. **a** Lookup table of the multi-pixel encoding strategy. **b** A segment that can encode a number between 0.2 and 0.3. **c** An example of a DMD binary pattern generated using this encoding strategy.

S5: The position of the focal spot in axis direction

In this experiment, a square capillary (100 µm × 100 µm) filled with the resin is used instead of the rectangular capillary. The SPAD is placed on the distal side of the diffuser (invasive focusing) for a faster optimization speed. After a focal spot is formed by the optimization, the objective MO_2 is aligned to image the focal plane of this spot. Then MO_2 is moved along the optical axis (*z*-axis) by a motorized stage and the transverse intensity profile at each *xy*-plane is recorded by a camera. Fig. S5a shows the longitudinal section of the focused beam profile. The z-position of this focal spot is set to 0 for comparison. After the measurement, MO_2 is moved back to the initial position (the focal plane of the initial spot). The sample is shifted in *y*-direction for 100 µm (beyond the optical memory effect) to position 2 to ensure that the focal spot will switch to another hot spot. After an optimization from scratch, the beam profile is measured again. Fig. S5b shows that this focal spot appears at the plane z = 25 µm. This means that MO_2 needs to be adjusted in *z*-direction for a relatively large range to find the focal plane of the spot. An easy solution is to use a 20-µm-thick resin confined by the rectangular capillary (20 µm × 200 µm). The axial feature size of the focal spot is 10~15 µm. Therefore, the focal spot is around the center of the capillary, making it easier to find the focal plane for imaging.

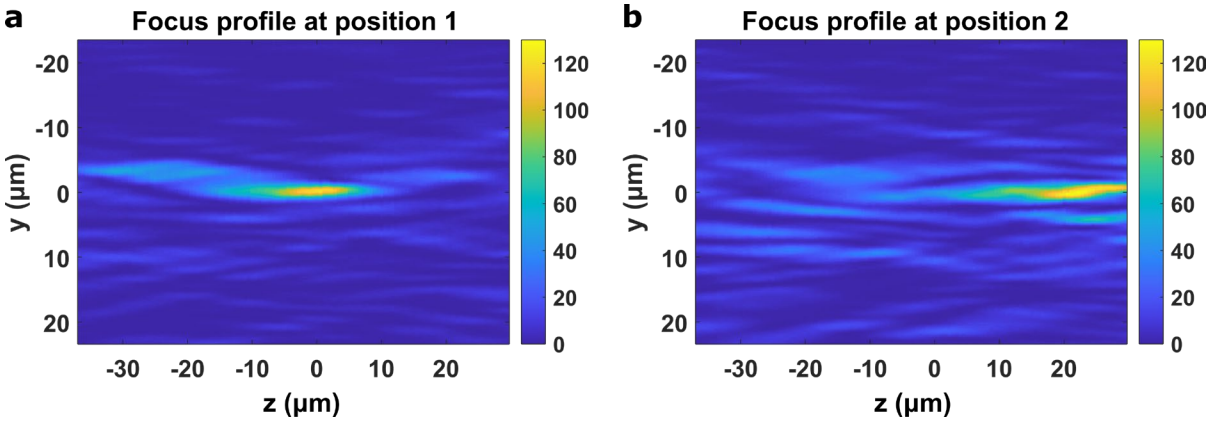

Fig. S5 a NIR beam profile in *yz*-plane at position 1. The focus position in *z*-direction is set as z = 0. Then the sample is shifted in the lateral plane to position 2. **b** NIR beam profile of the focusing result at position 2. Absolute values are used in the *z*-axis tick for comparison and relative values are used in the *y*-axis tick. It shows that the position of the focal spot can appear in a large range (at least ± 25 µm) in *z*-direction.

This practice does not affect the focusing and printing because the imaging system is only used for inspecting NIR patterns. However, a thicker resin results in more hot spots in the illuminated volume, which will slow the converging speed[3].

S6: Light dose distribution of sample shifting after one focusing process

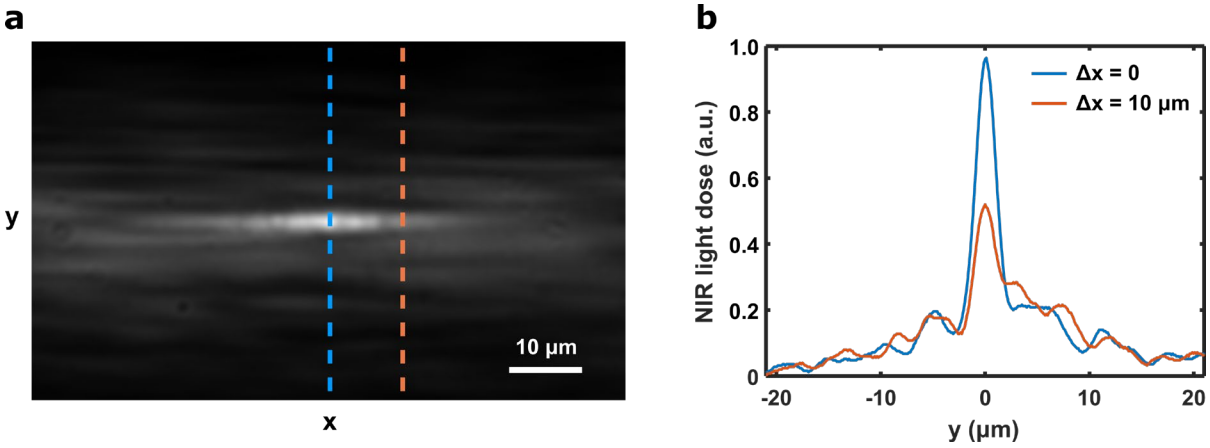

Fig. S6 a NIR light dose distribution after one focusing process followed by sample shifting in the *x*-direction. **b** Profile of the light dose along the dash lines marked in (**a**) at $\Delta x = 0$ (blue) and $\Delta x = 10$ μm (orange). The peak intensity as well as the contrast decreases significantly with the shifted distance.

S7: Responding speed of the fluorescent signal

The rise and decay dynamics are studied using 976-nm excitation pulses. We only studied the dynamics of the emission peak at 475nm due to the availability of the bandpass filter in our lab. In Fig. S7a, the excitation pulse starts at t = 0 and lasts 12.5 ms. The rise time is defined as the time between the initial rising moment and the moment reaching the plateau of the fluorescent emission. Effective decay time is defined by[4]:

$$\tau = \frac{\int_{t=initial\ decay\ moment}^{\infty}(t - initial\ decay\ moment)I(t)dt}{\int_{t=initial\ decay\ moment}^{\infty} I(t)dt} \quad (1)$$

At an excitation intensity of 10 MW/cm^2, the rise time is 0.18 ms and the decay time is 0.32 ms. At the intensity of 1.5 MW/cm^2, the rise time is 0.26 ms and the decay time is 0.33 ms. Multiple DMD patterns might contribute to the measured fluorescent signal when operating at a high display rate (1 kHz or higher).

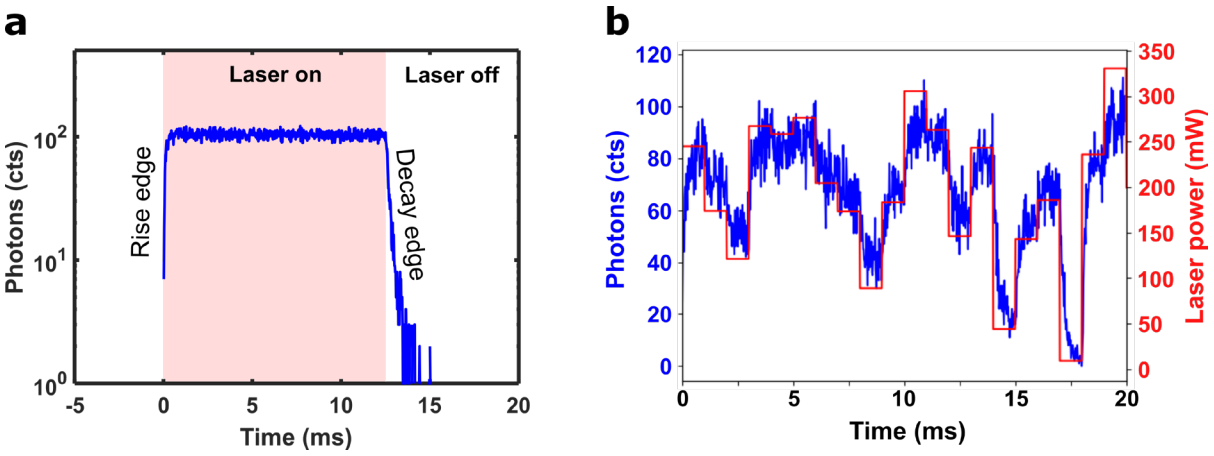

Fig. S7 a Rise and decay dynamics of the fluorescent peak at 475 nm. **b** Fluorescent signal response (475 nm) of random laser powers operated at 1 kHz.

We test the responding dynamics of the fluorescent signal using random laser powers modulated at 1 kHz. As the fluorescent intensity increases with the increase of laser power, by comparing the fluorescent signal curve with the laser power curve (Fig. S7b), we are able to check if the fluorescent output can reflect the change of input power. Although it takes time to reach a stable emission, the total fluorescence during the interval of two successive modulations does represent the change of the input power qualitatively. At higher frequencies (for example, 2 kHz), where the time interval (0.5 ms) is similar to the rise and decay time, the fluorescent signal will not be able to reflect the information of the speckle accurately.

S8: DPC microscopy

Because of the low refractive index mismatch (~0.001) between the polymerized and unpolymerized gelMA, all the printed parts in this study are imaged by a DPC microscope. It consists of a left-half and a right-half LED source. Fig. S8a shows the images taken with these two light sources separately. In the image taken with the left half source, bright edges can be seen on the left side of the printed structure and dark edges on the right side. Then sum of these two images is calculated to mimic the brightfield image and the difference (I_L-I_R) is calculated to obtain the DPC image. The printed object can hardly be seen in the brightfield image but is visible in the DPC image because the phase change is translated into intensity variation by the asymmetric light source. With light sources placed at the left and the right, the DPC image shows the best contrast in the horizontal direction. Therefore, the sample is placed at 45 ° to obtain a similar contrast across the whole structure. With the knowledge of the light source[5], the quantitative phase image is reconstructed from the DPC image and rotated by -45° for visualization (Fig. S8b). The effect of the optimization process on the obtained print can be seen from dark spots across the printed structures. Although optimized at low NIR power, the long optimization time during noninvasive printing contributes to the photopolymerization light dose, resulting in a larger phase change and, thus higher degree of polymerization. Print feature size is extracted and averaged from the FWHM of the phase profile.

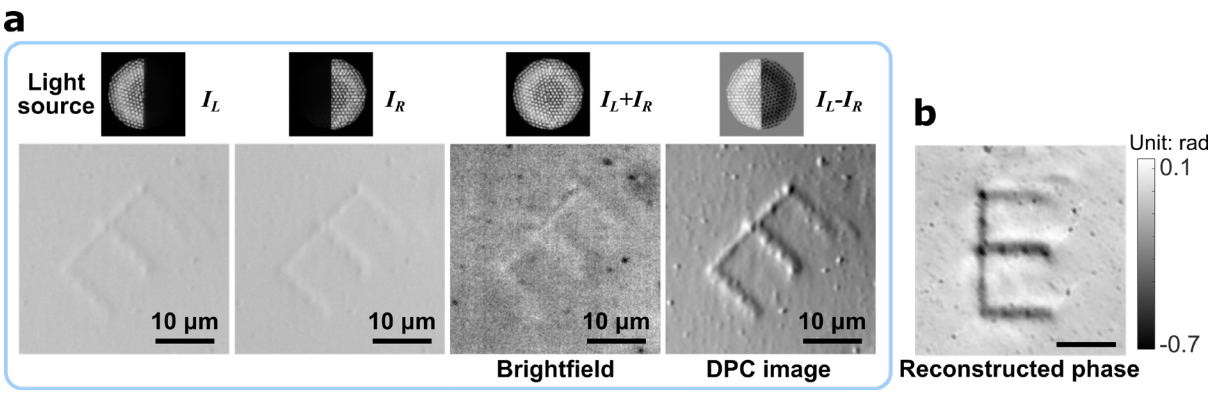

Fig. S8 a Intensity image taken with the left and right halves of the LED source. The brightfield image is generated by the sum of the two half-circle images and contains no phase contrast. The DPC image is the difference of the two half-circle images. **b** Reconstructed phase of the DPC image in (**a**) after rotating -45°. Scale bar: 10 μm.

S9: Biocompatibility of UCNPs

Cell viability experiment was conducted to demonstrate the biocompatibility of our UCNPs. The negative control group, UCNP group, and positive control group correspond to human foreskin fibroblasts (HFF-1) untreated, treated with UCNP solution (10 mg/mL), and with DMSO, respectively. There is no significant decrease in the cell viability of UCNP group compared to that of negative control group (Fig. S9a), indicating good cellular compatibility of our UCNPs. In contrast, fibroblasts viability was completely lost after the treatment with DMSO, confirming the expected cytotoxicity of this chemicals.

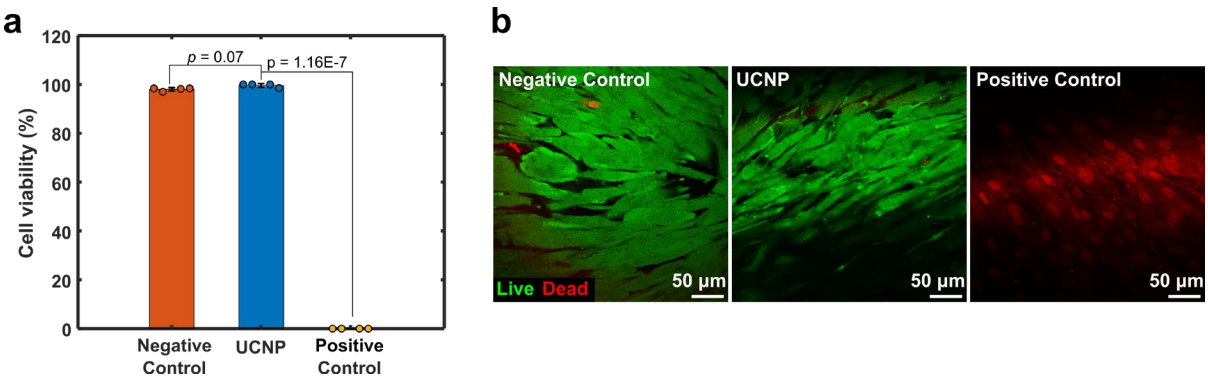

Fig. S9 a Cell Viability of fibroblasts untreated (negative control), treated with UCNP, and DMSO (positive control). n = 4 for all the treatment. Error bars represent standard deviation. p-values come from paired two-sided t-test. **b** Live/Dead assay of fibroblasts performed 48 h after treatment.

UCNPs dispersed in phosphate-buffered saline (PBS) at 10 mg/mL were filtered with a 0.22 μm filter. Human foreskin fibroblasts (HFF-1) cells were purchased from ATCC® and cultured in Dulbecco's Modified Eagle's Medium (DMEM) without phenol red, supplemented with 1%

Penicillin-Streptomycin (Gibco), 2% L-glutamine (Gibco) and 15% FBS (Gibco). Cells were maintained in a humidified CO_2 incubator at 37 °C and 5% CO_2. Cells were seeded in two 8-multiwell chambers at a cell density of 9.5×10^4 cells/cm^2 for 48 h. Then, culture medium was carefully removed, and 50 μL of culture medium, UCNP solution, and DMSO were added to different wells followed by 30 min treatment at 37 °C. After the treatment, 200 μL of culture medium was pipetted into each well and the chambers were kept in the incubator for 48 h. Three different replicas were considered for each group. All these manipulations were carried out under sterile conditions in a biosafety cabinet.

Live/Dead Assay was carried out to evaluate the HFF-1 viability. Specifically, the Live/Dead solution was prepared by adding ethidium homodimer-1 (Adipogen, CDX-E0512-M001, 2mM in DMSO) and fluorescein-AM (Merck, resuspended to 4mM in DMSO) to PBS in concentrations of 4 μM and 2 μM respectively. The solution was vortex-agitated for some seconds and kept at room temperature (RT) protected from light. Each well was then filled with 200 μL of Live/Dead solution. Imaging was conducted 30 min after staining and performed in a fluorescence confocal inverted microscope (Leica, SP8) with 25x NA 0.95 (Leica, HC PL Fluotar) objective. Specifically, fluorescein-AM was excited at 488 nm and its emission collected from 498 to 530 nm. Ethidium homodimer was excited at 540 nm. To avoid crosstalk with the emission spectrum of fluorescein-AM, the emission of Ethidium was collected from 560 nm to 618 nm. Microscope images were then processed and analyzed using ImageJ.

S10: The position switch of the focal spot

In invasive printing, the fluorescent signal is collected by the SPAD without scattering. The limited active area of the SPAD (d = 50 μm) results in a cylindrical collection volume of ~8 μm in diameter and 20 μm in height (resin thickness). Therefore, the focal spot only switches among the hot spots in this volume (Fig. S10a). In non-invasive printing, SPAD receives fluorescent signals from the whole speckle because of the scattering. The focal spot may switch to a position that is tens of microns away (mainly in the lateral direction) from the initial focal spot during dynamic focusing (Fig. S10b). Fig. S10c shows an example of the focal spot position switch during noninvasive printing. A vertical line was interrupted in the middle by the position switch and a second line was printed at a new position.

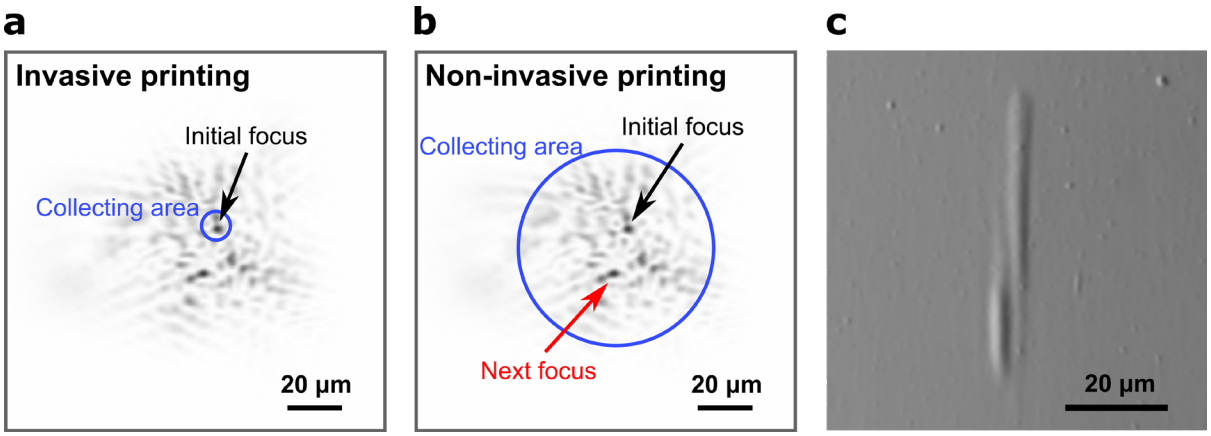

Fig. S10 Schematic diagram of the focal spot switching during invasive printing (**a**) and non-invasive printing (**b**). **c** A printed structure that was intended to be a 50-μm-long vertical line. A position switch of the focal spot can be observed during the printing.

S11: Optimization algorithm flow chart

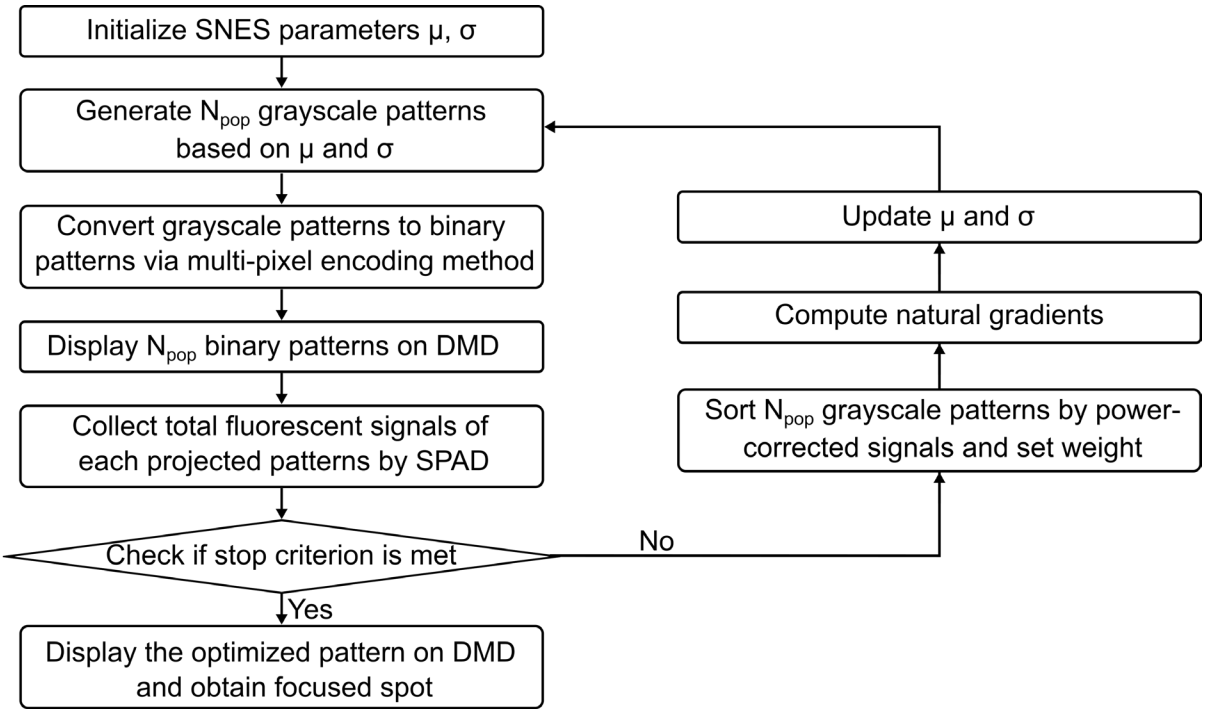

Fig. S11 Diagram of the optimization algorithm.

S12: Selection of optimization parameters

To speed up the printing process, it is essential to have a short optimization time. The optimization time is mainly limited by the pattern projection time (the time to project each generated pattern and receive feedback).

$$Total\ projection\ time \propto Total\ number\ of\ patterns = population \times iteration$$

The ideal intensity enhancement increases linearity with the number of segments. In practice, deviations from the ideal enhancement become significant at large segment number[6]. Additionally, larger segment number requires larger population number to converge. Fig. S12a shows the peak intensity of the NIR patterns inspected by the camera during the optimization using different segment number and population number. In segment number of 16×17, population number of ~40 is enough to ensure that population number is not a limiting factor of converging speed; in segment number of 80×85, a population number of ~160 is needed. With a fixed population number, for example, N_{pop}=40, larger segment number results in slower converging speed. Peak intensities versus total number of patterns are shown in Fig. S12b, indicating the relationship between enhancement and total optimization time. Segment number of 16×17 exhibits fast converge speed but relatively low enhancement. Segment number of 32×17 shows low converge speed because of insufficient population number. Segment number of 32×17, population number of 40 is the best choice to balance the enhancement and the optimization speed.

All the optimizations are conducted at the same position of the holographic diffuser to ensure that the optimization results are comparable. In each parameter set, the optimization was repeated 5 times with random initial population patterns to eliminate the potential effect of initial patterns.

a

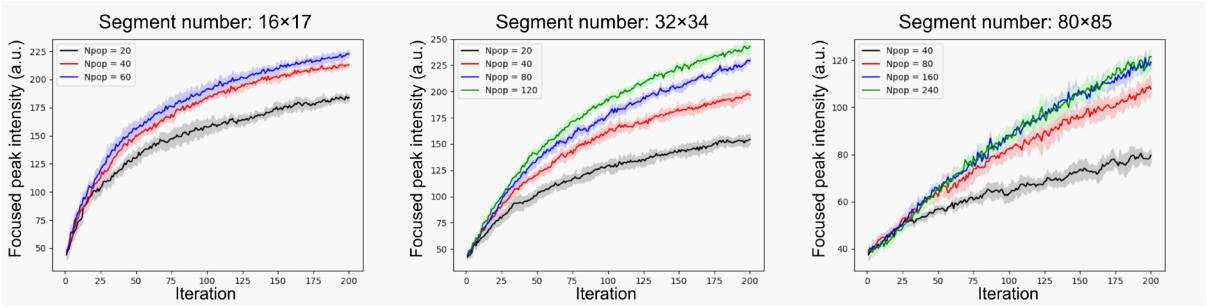

b

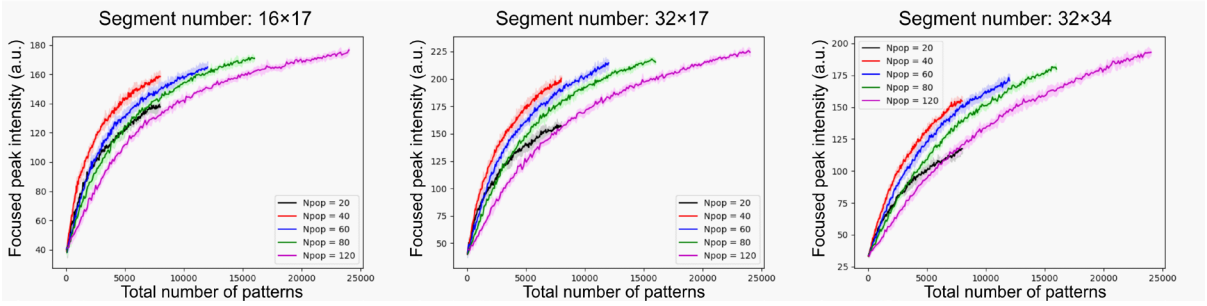

Fig. S12 Peak intensities of the NIR patterns inspected by the camera during the optimization versus iteration (**a**) and versus total number of patterns (**b**). Npop, population number.

S13: Distribution of UCNPs in the resin

The distribution of UCNPs in the resin is qualitatively measured optically because its optical performance can significantly affect the efficiency of the focusing process. Figure S13a shows the setup for measuring the fluorescent beam profile to check the dispersion of UCNPs in the resin. A continuous-wave laser at 976 nm (900 mW, BL976-PAG900, Thorlabs) with a Polarization-Maintaining (PM) optical fiber is collimated by a lens (F230APC-980, Thorlabs, f = 4.55 mm) and focused by a MO_1 (M Plan Apo NIR 20X, Mitutoyo) into a glass square capillary (300 μm ×300 μm, CM Scientific). As the beam (d = 1 mm) does not fill the aperture of the back focal plane of the objective MO_1, the focused beam has a beam waist of 11 mm (FWHM) with a low numerical aperture (NA ~ 0.05). The beam is almost collimated within the size of the capillary, providing a constant NIR intensity as well as a large volume of illumination. The capillary is filled with resin containing UCNP (10 mg/mL) and gelMA (15 wt%). The fluorescence is collected via MO_2 (UApo/340 20x, Olympus) and a lens (f = 200 mm) and recorded by Cam (BFS-U3-31S4M, FLIR). The NIR light is cut off by a short-pass (SP) filter (FESH0600, Thorlabs).

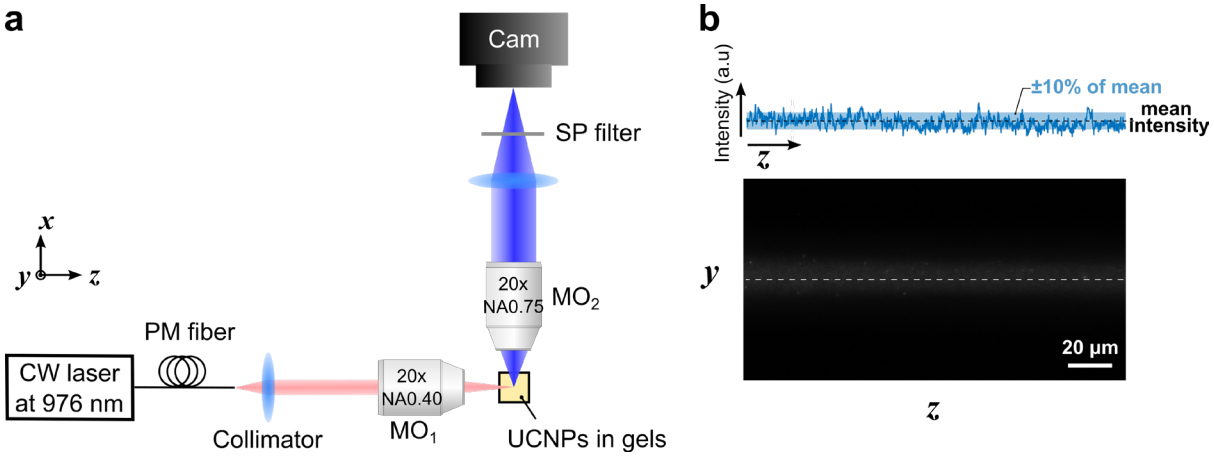

Fig. S13 (**a**) Experimental setup for imaging the fluorescent beam profile. (**b**) An example of the fluorescent beam profile at the *yz*-plane. The blue curve on the top of the image shows the fluorescent intensity profile along the white dashed line. The shadow behind the curve shows ±10% of the mean value of the profile.

Fig. S13b shows the fluorescent beam profile at the *yz*-plane. The fluorescent emission is relatively smooth along the NIR beam. The mean and standard deviation of the fluorescent intensity profile along the dashed line is 36.0 ± 3.1. Several hotspots may result from small clusters, but the spot size is quite small (<1 μm) and the light intensity is not significant

compared to that of the background, indicating that the dispersion of UCNPs in the resin is uniform enough for our printing technique.

S14: Optical response of UCNPs during long illumination time

The spectra of UCNPs in the gelMA solution are measured during a 1-hour illumination time to verify its optical response during the printing process. It is measured with a modified setup of the one in Fig. S13a. The fluorescence is collected via MO_2 (UApo/340 20x, Olympus) and a lens (LA4052-A-ML, Thorlabs, f = 35 mm) and recorded by a spectrometer (Ocean Optics USB4000, Ocean Insight). The NIR light is cut off by a short-pass filter (FF01-720/SP-25, Semrock). The excitation intensity is 1.5×10^4 W/cm^2, the approximate NIR intensity during the printing process, and the spectra are recorded after 0, 30, and 60 min of illumination (Fig. S14). No significant decrease in emission intensity or change of spectrum shape can be observed, indicating the non-bleaching feature of UCNPs and their stable optical response during the whole additive manufacturing process.

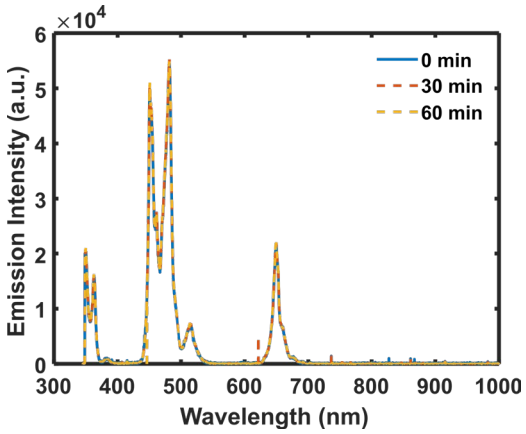

Fig. S14 Emission spectra of UCNP under 976-nm light illumination of 0, 30, and 60 min.

S15: Video of the NIR dose distribution during invasive printing of "EPFL"

The video is generated by summing up the NIR patterns based on the shifted position. It is played at 125× of the original printing speed. The focusing process is ignored because it is done at much lower laser power. Fig. S15 shows the last frame of this video.

Fig. S15 Last frame of the video. It shows the final NIR dose distribution of the printing.

Reference

[1] Li, F., Tu, L., Zhang, Y., Huang, D., Liu, X., Zhang, X., Du, J., Fan, R., Yang, C., et al., "Size-dependent lanthanide energy transfer amplifies upconversion luminescence quantum yields," Nature Photonics1–10 (2024).

[2] Würth, C., Fischer, S., Grauel, B., Alivisatos, A.P., and Resch-Genger, U., "Quantum Yields, Surface Quenching, and Passivation Efficiency for Ultrasmall Core/Shell Upconverting Nanoparticles," Journal of the American Chemical Society 140(14), 4922–4928 (2018).

[3] Osnabrugge, G., Amitonova, L.V., and Vellekoop, I.M., "Blind focusing through strongly scattering media using wavefront shaping with nonlinear feedback," Optics Express 27(8), 11673–11688 (2019).

[4] Vetrone, F., Boyer, J.-C., Capobianco, J.A., Speghini, A., and Bettinelli, M., "Significance of Yb3+ concentration on the upconversion mechanisms in codoped Y2O3:Er3+, Yb3+ nanocrystals," Journal of Applied Physics 96(1), 661–667 (2004).

[5] Bonati, C., Loterie, D., Laforest, T., and Moser, C., "Lock-in incoherent differential phase contrast imaging," Photonics Research 10(1), 237–247 (2022).

[6] Akbulut, D., Huisman, T.J., Putten, E.G. van, Vos, W.L., and Mosk, A.P., "Focusing light through random photonic media by binary amplitude modulation," Optics Express 19(5), 4017–4029 (2011).